RSC Advances

ROYAL SOCIETY OF CHEMISTRY

www.rsc.org/advances

Journal Name

RSCPublishing

ARTICLE

Co_9S_8 nanoparticles encapsulated in nitrogen-doped mesoporous carbon networks with improved lithium storage properties

Cite this: DOI: 10.1039/xoxxooooox

Received ooth January 2012,
Accepted ooth January 2012

DOI: 10.1039/xoxxooooox

www.rsc.org/

Jawayria Mujtaba [a, †], Hongyu Sun [*a, b, †], Guoyong Huang [c, d], Yanyan Zhao [a], Hamidreza Arandiyan [e], Guoxing Sun [f], Shengming Xu [c], Jing Zhu [*a]

We report the designed synthesis of unique Co_9S_8 nanoparticles encapsulated in nitrogen-doped mesoporous carbon networks (Co_9S_8@NMCN nanocomposites). Uniform zeolitic imidazolate framework-67 are first synthesized and then transformed into Co_9S_8@NMCN nanocomposites by thermal annealing with sulfur powders in Ar atmosphere. The structural and compositional analysis are conducted by employing X-ray diffraction (XRD), scanning electron microscopy (SEM), transmission electron microscopy (TEM), and X-ray photoelectron spectroscopy (XPS), which show that each Co_9S_8 nanoparticle is well encapuslated in nitrogen-doped carbon layers. When evaluated as anode material for LIBs, the as-prepared composite electrodes delivered superior capacity, excellent cycling stability and rate capability, which are attributed to the advantageous structural features.

1. Introduction

Rechargeable lithium-ion batteries (LIBs) with the advantages of low self-discharge rate, high operating voltage, and no memory effect have shown important applications in typical energy storage systems, such as mobile electronics, electric vehicle, energy source for large-scale electric energy storage technologies and so on.[1-3] Developing advanced cathodes and anodes electrode materials is a key element in achieving the required performance and capacity of LIBs for the above mentioned important applications, since the overall performance of LIBs is highly dependent on the inherent electrochmical properties of the electrode materials.[4,5] Current commercial anode material, *i.e.*, graphite, cannot meet the requirements of high-performance LIBs because of its low theoretical capacity (372 $mAhg^{-1}$) and serious safety problems arising from low Li^+ intercalation potential.[6] So far, alternative anode materials, such as alloys,[7,8] transition-metal carbides,[9,10] nitrides,[11,12] oxides,[13] and sulfides[14,15] have been exploited to exhibit better electrochemical performances.

Among those materials, transition metal sulfides have received considerable attention since they can exhibit high theoretical capacities, low cost and widespread availability in the world.[16-18] Typically, the family of cobalt sulfides shows relatively good electrical conductivities, fair thermal stabilities and high theoretical capacities.[19,20] They can electrochemically react with lithium through conversion mechanism to form metallic cobalt and Li_2S and deliver high theoretical capacities. The reaction can be described as $CoS_x + 2xLi^+ + 2xe^- \leftrightarrow Co + xLi_2S$. Unfortunately, the employment of cobalt sulfides in high performance LIBs is largely hampered by the pronounced volume change and particle aggregation with the Li insertion and extraction processes, which often lead to electrode pulverization and loss of effective contact between the particles and in turn lead to the fast capacity fading and poor cycling stability.[21,22] Moreover, unsatisfactory electrochemical performance caused by sluggish ion/electron transport kinetics also impedes their applications.

The constructions of nanostructured materials with proper morphology, composition, and microstructure offer a great opportunity to enhance the lithium storage properties of cobalt sulfides. The nanostructures as compared to their bulk counterparts can provide more active sites for the storage of lithium ions, facilitate electron and lithium ion transport, accommodate the local volume change upon charge/discharge cycling and are able to alleviate the problem of pulverization and aggregation of the electrode materials.[23-25] Therefore, nanostructured electrodes generally lead to improved energy density, better capacity retention, and superior rate capability. For instance, Co_9S_8 nanotubes prepared in terms of the nanoscale Kirkendall effect presented a high initial discharge capacity.[26] Hollow nanospheres of mesoporous Co_9S_8 were successfully synthesized by a facile solvothermal reaction followed with a high-temperature annealing. These hollow nanoparticles exhibited a reversible capacity of ~1414 $mAhg^{-1}$ after 100 cycles at 100 mAg^{-1}.[27]

Comparing with lithium metal and carbonaceous materials, the conductivity of cobalt sulfides is inferior, which seriously restricts their applications in high-rate rechargeable batteries. Coating the electrochemically active materials with an electronically conductive agent layer can not only enhance the conductivity of the electrode materials but also modify the chemistry at the electrode/electrolyte interface, which is considered as an effective approach to improve the cycling stability and rate capability.[28-32] For example, Huang *et al*[32] synthesized cobalt sulfides/graphene composites through a

facile one-pot solvothermal method. The sphere-like cobalt sulfide particles with uniform size were highly dispersed on or wrapped in the creasy graphene. The cobalt sulfides/graphene composites displayed much higher reversible capacity of about 1010 $mAhg^{-1}$ with better rate capability and excellent cyclic stability than the cobalt sulfides, hereby, demostrating the importance of graphene addition. We previously also demostrated that carbon nanotube or graphene based metal oxides and sulfides possessed higher lithium storage capacity and better rate capability.[33-37]

In this work, we demonstrate a facile approach for the synthesis of Co_9S_8 nanoparticles encapsulated in nitrogen-doped mesoporous carbon networks (Co_9S_8@NMCN nanocomposites). This strategy involves the facile synthesis of zeolitic imidazolate framework-67 (ZIF-67) crystals,[38,39] which is a typical metal organic framework (MOF), and subsequent thermal annealing with sulfur powders in Ar atmosphere. We find that the obtained products well maintain size homogeneity and structural morphology of the initial ZIF-67 crystals, and Co_9S_8 nanoparticles are completely encapsulated by nitrogen-doped carbon layers. The mesoporous network structures provide additional free room to accommodate the local volume change upon charge/discharge cycling, and sufficient active sites for the storage of lithium ions. Furthermore, the electron transportation can be enhanced through the NMCN. As a consequence, the yielded Co_9S_8@NMCN nanocomposites exhibit a maximum reversible specific capacity of 988 $mAhg^{-1}$ at a current density of 0.1 Ag^{-1} with outstanding charge/discharge rate capability and good cycling performance, demonstrating a great potential as anode materials for LIB applications. Our work presents a facile technique for the preparation of other metal sulfides/carbon nanocomposites that hold great promise in the field of energy storage and conversion.

2. Experimental

2.1 Materials synthesis

Synthesis of ZIF-67 Crystals. All the chemicals were used directly without further purification. In a typical synthesis, two solutions were prepared by dissolving 5 mmol of $Co(NO_3)_2{\cdot}6H_2O$ and 20 mmol of 2-methylimidazole in 30 ml of methanol, respectively. The solution of 2-methylimidazole was then quickly poured into the solution of $Co(NO_3)_2{\cdot}6H_2O$ and the resultant mixed solution was aged for 24 h at room temperature. The purple precipitates were collected by centrifugation and dried at 70 °C for 6 h.

Synthesis of Co_9S_8@NMCN nanocomposites. In a typical procedure, a thoroughly mixed powder with 0.2 g ZIF-67 crystals and 0.1 g S powders were put into a tube furnace and then heated up to 600 °C at the rate of 2 °C min^{-1} and maintained at this temperature for 2 h under an argon gas flow of 60 ml min^{-1}. After the furnace was completely cooled, the product was taken out for further characterizations. Meanwhile, control experiments were performed to synthesize Co_9S_8 nanoparticles by a hydrothermal process as reported elsewhere.

2.2 Materials characterization

Crystallographic information for the samples was collected using a Bruker Model D8 Advanced powder X-ray diffractometer (XRD) Cu K_α irradiation (λ = 1.5418 Å). The morphology and microstructure of the products were examined using field-emission scanning electron microscopy (FESEM; Hitachi-S5500, 5 kV), transmission electron microscopy (TEM; JEOL, JEM-2100, 200 kV), X-ray photoelectron spectroscopy (XPS, Escalab 250, Al Kα), Raman microscopy (Renishaw, UK, 633 nm excitation), and thermal gravimetric (TG) analysis (Netzsch-STA 449C, measured from room temperature to 600 °C at a heating rate of 10 °C min^{-1} under an air flow). The Brunauer-Emmett-Teller (BET) surface area of the powders was analyzed by nitrogen adsorption-desorption isotherm at 77 K in a Micromeritics ASAP 2010 system. The sample was degassed at 180 ºC before nitrogen adsorption measurements. The BET surface area was determined by a multipoint BET method. A desorption isotherm was used to determine the pore size distribution via the Barret-Joyner-Halender (BJH) method, assuming a cylindrical pore model. The nitrogen adsorption volume at the relative pressure (P/P_0) of 0.994 was used to determine the pore volume and average pore size.

2.3 Electrochemical measurements

The working electrodes were constructed by mixing the active materials, conductive carbon black and carboxymethyl cellulose, in a weight ratio of 80:10:10. The mixture was prepared as slurry and spread onto copper foil. The electrode was dried under vacuum at 120 °C for 6 h to remove the solvent before pressing. Then the electrodes were cut into disks (12 mm in diameter) and dried at 100 ºC for 24 h in vacuum. The cells were assembled inside an Ar-filled glove box by using a lithium metal foil as the counter electrode and the reference electrode and microporous polypropylene as the separator. The electrolyte used was 1M Lithium hexafluorophosphate ($LiPF_6$) dissolved in a mixture of ethylene carbonate (EC), propylene carbonate (PC), and diethyl carbonate (DEC) with a volume ratio of EC/PC/DEC = 1:1:1. Assembled cells were allowed to soak overnight, and then electrochemical tests on a LAND battery testing unit were performed. Galvanostatic charge and discharge of the assembled cells were performed at a current density of 0.1 Ag^{-1} between voltage limits of 0.01 and 3.00 V (vs. Li^+/Li) for 80 cycles. For the high rate testing, the discharge current gradually increased from 0.1 Ag^{-1} to 0.2, 0.5, and 1 Ag^{-1}, and then decreased to 0.1 Ag^{-1}, step by step. All the charge/discharge testings were performed symmetrically at room temperature. The cyclic voltammogram (CV) was performed using a CHI 660D electrochemical workstation (Chenhua Instrument, Shanghai). CV curves were recorded between 0.01 and 3.00 V (vs. Li^+/Li) at a scan rate of 0.5 mV s^{-1}. Electrochemical impedance spectroscopy (IM6, Zahner) was carried out by applying an AC voltage of 5mV over a frequency range of 100 kHz to 0.01 Hz.

3. Results and discussion

FESEM image (Fig. S1†) reveals that the ZIF-67 precursor particles show a polyhedral shape with a smooth surface and an average size of approximately 1 μm. Powder XRD result shows all diffraction peaks with strong intensities match well with the simulated ZIF-67,[40] indicating the pure phase and high crystallinity of ZIF-67 particles (Fig. S2†). The Co_9S_8@NMCN nanocomposites are obtained by thermal annealing the ZIF-67 particles with sulfur powders in Ar atmosphere. To check the phase purity and crystallographic structure of the products, XRD was performed as shown in Fig. 1. All the diffraction peaks can be perfectly identified as the Co_9S_8 phase (JCPDS No. 19-0364). No other diffraction peaks from possible impurities are observed, indicating the high phase purity of the products. The relatively high peak intensities imply that the products are highly crystalline. The crystallite sizes (d) of Co_9S_8 nanoparticles can be estimated from the physical

breadths of the corresponding diffraction peak by the Scherrer formula: $d = 0.89\lambda/\beta\cos\theta$, where λ is the X-ray wavelength, β the full width at half maximum of the diffraction peak, and θ is the Bragg diffraction angle.[41,42] The average crystallite size was yielded to be ~25.8 nm by using (440) peak. This is further confirmed by TEM observations as discussed later.

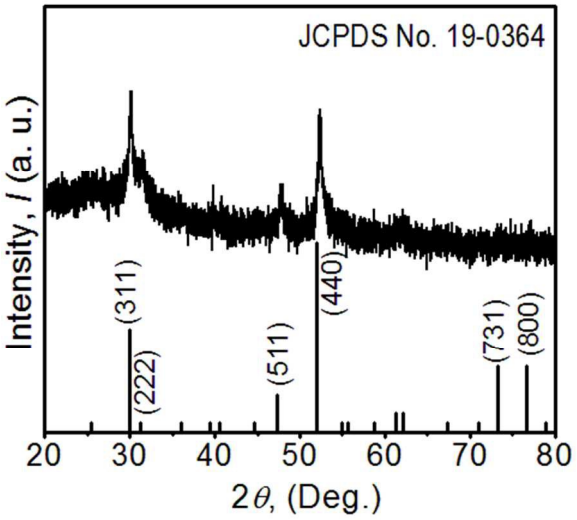

Fig. 1. XRD pattern of as-prepared sample and standard pattern of cubic phase Co_9S_8.

Typical FESEM image (Fig. 2a) show that the nanoparticles are uniformly distributed on the substrate, which is similar to the ZIF-67 precursors, implying that the annealed products have well maintained size homogeneity and structural morphology of ZIF-67 crystals even after undergoing a high-temperature annealing process. Higher magnification FESEM image (Fig. 2b) indicates that the particle surface is rough and possesses many tiny holes, which can be ascribed to the decomposition of the precursors and the liberation of CO_2 and H_2O during thermal treatment.

The detailed structural information of the composites is carried out by employing TEM and HRTEM characterizations. Fig. 2c shows a typical TEM image of Co_9S_8@NMCN nanocomposites with outlines similar to the original ZIF-67 crystals. High density of nanoparticles is uniformly dispersed on continuous ultrathin substrate in a single large particle, which is beneficial for maintaining a large specific surface area. Statistical analysis over 200 nanoparticles for the sample provides that the mean size of the nanoparticles is ~27.3 nm, which is in agreement with XRD results (Fig. S3†). EDX analysis (Fig. S4†) shows that the nanoparticles are composed of Co and S with an atomic ratio of ~1:1, further confirming the formation of Co_9S_8 (Cu peaks come from the copper grid that used to support the sample for TEM observations). Fig. 2d-f shows three typical Co_9S_8@NMCN nanocomposites with different orientations. There are numerous holes in each particle, demonstrating the porous nature of the products. The selected area electron diffraction (SAED) pattern indicates that the as obtained Co_9S_8@NMCN nanocomposites are polycrystal in nature (Fig. 2g), and the diffraction rings can be indexed to the (311), (511), (440), and (731) planes of Co_9S_8 (JCPDS No. 19-0364). Fig. 2h-i show typical HRTEM images of Co_9S_8@NMCN nanocomposites. The lattice spacings are determined to be ~2.71 Å, ~2.77 Å, ~2.28 Å and ~2.30 Å, which correspond to the (222) and (331) planes of Co_9S_8 phase. It can be clearly seen that all the Co_9S_8 nanoparticles (see the black arrows) are completely coated by carbon layers (see the red arrows). Furthermore, those carbon layers form a continuous mesoporous network, which is of great importance to enhance the conductivity, and efficiently use each Co_9S_8 nanoparticles in the composites. The above results show that we succeeded in synthesizing Co_9S_8@NMCN nanocomposites by a facile thermal annealing MOF precursor with sulfur powders at high temperature.

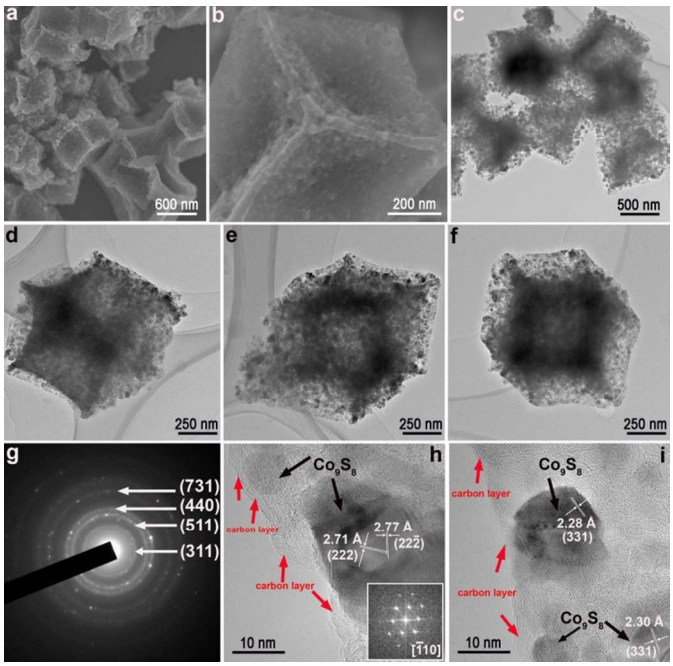

Fig. 2. (a, b) FESEM images, (c-i) TEM, HRTEM images and SAED pattern of the Co_9S_8@NMCN nanocomposites. The red and black arrows in (h, i) show the existence of carbon layers, and the encapsulated Co_9S_8 nanoparticles, respectively. The inset in (h) shows corresponding FFT image of the larger Co_9S_8 nanoparticles.

The surface chemical composition and electronic states of the Co_9S_8@NMCN nanocomposites are analyzed by using XPS in the range of 0-1350 eV. The survey spectrum (Fig. S5†) shows obvious XPS peaks of cobalt, sulfur, carbon, and nitrogen, confirming the existence of those elements in Co_9S_8@NMCN nanocomposites, which is in good agreement with previous EDS analysis. Fig. 3a shows the high-resolution XPS spectra of Co 2p, which is best fitted with two spin-orbit doublets and two shakeup satellites. The doubles are characteristic of the peaks of Co^{2+} and Co^{3+}.[43] In the S 2p XPS spectrum (Fig. 3b), the raw curve is peak-fitted into four curves corresponding to three different types of sulfur species.[26,44] The

peaks at 161.5 and 163.0 eV can be assigned to the $2p_{3/2}$ and $2p_{1/2}$ core levels of S^{2-} in Co_9S_8, while the peaks at 164.5 and 167.7 eV can be attributed to the C–S–C and sulfur satellite peak. From the fine spectrum of C1s in the nanocomposites (Fig. 3c), three wide peaks are seen at 284.4, 285.4, and 287.6 eV, which are due to the C-C bond, C-S, and C-O-C bond, respectively.[44-46] The C–S peak is attributed to the single bonds between the Co_9S_8 and the carbon.[45,46] The bonding state of N atom in the composite is studied by deconvoluting high-resolution N1s spectrum as shown in Fig. 3d. The peaks centered at 397.8, 398.6, 400.4, and 404.7 eV can be assigned as pyridinic N, pyrrolic N, quaternary N, and N-oxides of pyridinic N, respectively.[47] Nitrogen doping can enhance the conductivity of the carbon layers in the composites, which is the key to improve the rate performance of the electrode materials.[47, 48]

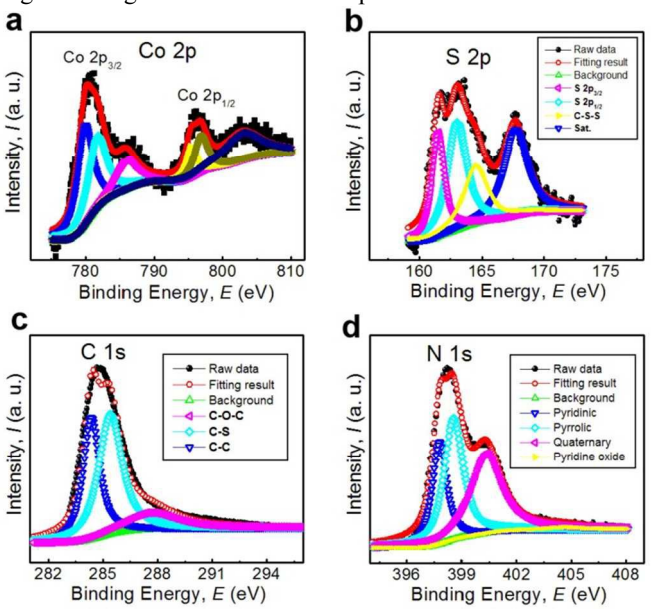

Fig. 3. High-resolution XPS spectra of the as obtained Co_9S_8@NMCN nanocomposites. (a) Co 2p, (b) S 2p, (c) C 1s, and (d) N 1s regions.

The Raman spectrum of Co_9S_8@NMCN nanocomposites can be divided into two parts (Fig. 4a). There are a few strong Raman bands below 1000 cm^{-1} which can be indexed to Co_9S_8.[45] The Raman bands above 1000 cm^{-1} are indexed to carbon layer. Specifically, the peak at 1334.9 cm^{-1} (*D* band) is a disordered band associated with structural defects, amorphous carbon or edges that can break the symmetry and selection rule, while the peak at 1577.3 cm^{-1} (*G* band) is attributed to the vibration of sp^2 hybridized C–C bond of an in-plane hexagonal lattice. The ratio of the *D* band peak intensity to that of the *G* band peak intensity I_D/I_G value is ~1, indicating the formation of numerous defect structures in the carbon matrix, which may be due to the nitrogen doping effect. The amount of NMCN in the composites is determined through TG experiment (Fig. S6†). The weight loss before 200 °C could be ascribed to surface water adsorption, while the weight loss after ~250 °C could be ascribed to the gradual oxidation of carbon and Co_9S_8 phase in the nanocomposites, which yielding the weight fraction of rGO in the nanocomposites of about 47% (Fig. S6, 7†). The presence of NMCN in the composites could dramatically enhance the electronic conductivity of Co_9S_8 nanoparticles and is responsible for improving lithium storage properties.

The specific surface areas and the porous feature of the Co_9S_8@NMCN nanocomposites are studied by measuring nitrogen adsorption–desorption isotherms at 77 K (Fig. 4b). The specific surface area of the nanocomposites is calculated to be 76.9 m^2g^{-1} by using the BET method. Although the surface area of Co_9S_8@NMCN composites is relatively low in view of a mesoporous material containing carbon, the value is still higher than or comparable with typical mesoporous Co_9S_8 and Co_9S_8/carbon nanostructures, for example, hierarchical hollow Co_9S_8 microspheres (80.38 m^2g^{-1}),[49] Co_9S_8-carbon composite (78.2 m^2g^{-1}),[29] mesocrystal Co_9S_8 hollow sphere (52.6 m^2g^{-1}),[50] hollow nanospheres of mesoporous Co_9S_8 (26 m^2g^{-1}),[51] and yolk-shell Co_9S_8 microspheres (18 m^2g^{-1}).[52] In addition, the narrow micro- and mesopore size distribution based on the BJH method of the sample is further confirmed by the corresponding pore size distribution curve (the inset of Fig. 4b). The peak centered at ~1.7 and ~3.9 nm reveals that uniform micro- and mesopores dominate in the composites. The large surface area and narrow pore size distribution of the sample are due to the porous nature of the micro/nanoarchitectures. The microstructure characteristics of the Co_9S_8@NMCN nanocomposites are favourable to be used as anode materials in LIBs due to the capability of providing extra active sites for the storage of lithium ions, accommodating the local volume change during cycling, and facilitating mass diffusion and ion transport.

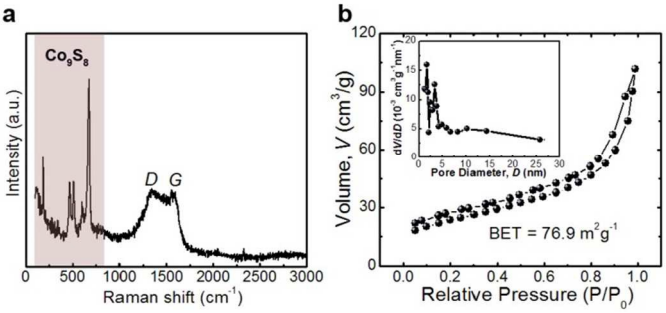

Fig. 4. (a) Raman spectrum and (b) nitrogen adsorption–desorption isotherms of the Co_9S_8@NMCN nanocomposites. The inset in (b) is the corresponding pore size distribution curve.

The electrochemical behaviour of the Co_9S_8@NMCN nanocomposites is first investigated by CV experiments between 0.01 and 3.00 V vs. Li^+/Li at a scan rate of 0.5 mVs^{-1}. Fig. 5a shows the CV curves of Co_9S_8@NMCN nanocomposites for the first three cycles. In the first cycle, the strong cathodic peak at ~1.06 V is due to the reduction of Co_9S_8 to metallic Co, and the peak at ~0.77 V is related to the formation of solid electrolyte interface (SEI) layer on the

electrode surface and Li_2O. The anodic peaks at 2.07 V and 2.47 V are attributed to the reversible oxidation from Co^0 to CoS_x. The CV results are in good agreement with the previous reports.[53-55] In the subsequent two cycles, the CV curves overlap very well, indicating high electrochemical reversibility. The charge-discharge voltage profiles of the Co_9S_8@NMCN nanocomposites for the first three cycles at a current rate of 0.1 Ag^{-1} is shown in Fig. S8†. In the first discharge curve, there is a dominant potential plateau (~1.07 V) and a following slope, which represents lithium ion insertion process, and the formation of SEI film,[53,54] respectively. The initial discharge and charge capacities of the Co_9S_8@NMCN nanocomposites are 1705 $mAhg^{-1}$ and 1125 $mAhg^{-1}$, yielding the Coulombic efficiency of 66%. Such initial irreversible capacity loss should mainly originate the formation of SEI layer due to the irreversible degradation of electrolyte, the trapping of lithium inside the active material, the electrolyte decomposition catalyzed by Co, and so on, which is common for electrode materials based on conversion reaction mechanism.[56,57]

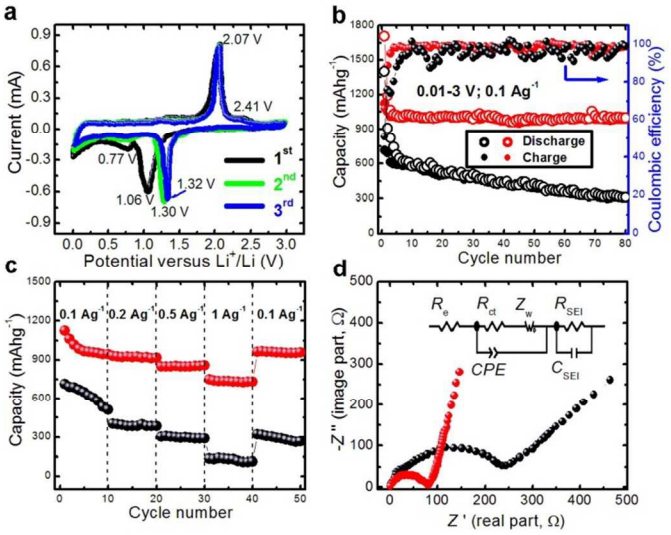

Fig. 5. Electrochemical performance of the Co_9S_8@NMCN nanocomposites: (a) CVs at a scan rate of 0.5 mVs^{-1} between 0.01 and 3 V, (b) cycling performance and (c) rate capability of the Co_9S_8@NMCN nanocomposites (red lines) and Co_9S_8 nanoparticles (black lines) electrodes, (d) Nyquist plots of the Co_9S_8@NMCN nanocomposites (red lines) and Co_9S_8 nanoparticles (black lines) electrodes measured with an amplitude of 5 mV over the frequency range of 100 kHz and 0.01 Hz. The inset shows the equivalent electrical circuit. R_e is the electrolyte resistance, R_{ct} is the charge-transfer resistance, Z_w is the Warburg impedance related to the diffusion of Li ions into the bulk electrodes, and *CPE* is the constant phase-angle element, involving double layer capacitance, R_{SEI} and C_{SEI} are the pseudocapacitance and resistance of SEI film, respectively.

Fig. 5b illustrates the charge/discharge capacity together with the Coulombic efficiency of Co_9S_8@NMCN nanocomposites and Co_9S_8 nanoparticles as function of the cycle number at a current density of 0.1 Ag^{-1} between 0.01 and 3 V vs Li^+/Li. It shows that the Co_9S_8@NMCN nanocomposites electrode exhibits a much better cycling performance than Co_9S_8 nanoparticles electrode. The Co_9S_8@NMCN nanocomposites exhibit excellent cyclic capacity retention from the first few cycles onwards. A reversible capacity ~988 $mAhg^{-1}$ can be retained at the end of 80 charge-discharge cycles. For comparison, the reversible capacity of Co_9S_8 nanoparticles decreases to 308 $mAhg^{-1}$ after 80 cycles of operation. It should be mentioned here that the measured reversible capacity for Co_9S_8@NMCN electrodes was higher than the theoretical value for Co_9S_8 (~540 $mAhg^{-1}$). Similar results have also been reported for other nanostructured metal oxide/sulfide electrodes,[23-25, 27] where surface storage for lithium ions plays an important role in the overall capacity. In our case, the porosity nature of the Co_9S_8@NMCN electrode can provide extra sites for the lithium surface storage during cycling, therefore a higher capacity larger than the theoretical capacity can be delivered. On the other hand, the reversible formation/dissolution of a polymeric gel-like film due to the degradation of electrolyte, which is typical in the electrodes based on conversion mechanism,[27, 58] also contributes to the additional capacity. The high reversible capacity and excellent cycling behaviour of the Co_9S_8@NMCN nanocomposites are also validated in the rate capability. Fig. 5c shows the capacity of Co_9S_8@NMCN nanocomposites and Co_9S_8 nanoparticles at different rates ranging from 0.1 Ag^{-1} to 1 Ag^{-1}. The Co_9S_8@NMCN nanocomposites electrode shows much better rate capability than Co_9S_8 nanoparticles. The reversible capacities of Co_9S_8 nanoparticles tested at 0.1 Ag^{-1}, 0.2 Ag^{-1}, 0.5 Ag^{-1}, and 1 Ag^{-1} are 510 $mAhg^{-1}$, 383.8 $mAhg^{-1}$, 290.8 $mAhg^{-1}$, and 112 $mAhg^{-1}$, respectively. The Co_9S_8@NMCN nanocomposites deliver reversible capacity of 943 $mAhg^{-1}$ at 0.1 Ag^{-1}, 914.9 $mAhg^{-1}$ at 0.2 Ag^{-1}, 856.1 $mAhg^{-1}$ at 0.5 Ag^{-1}, and 731.3 $mAhg^{-1}$ at 1 Ag^{-1}. When the current density reverses back to the original low rate of 0.1 Ag^{-1}, the capacity of the Co_9S_8@NMCN nanocomposites can recover to 957 $mAhg^{-1}$. Electrochemical impedance spectra (EIS) are measured to understand the Li^+ transfer behaviour in Co_9S_8@NMCN nanocomposites and Co_9S_8 nanoparticles. As shown in Fig. 5d, The Nyquist plots in the frequency range from100 kHz to 0.01 Hz consist of a depressed semicircle at the high to medium frequencies connected to a slope at the low frequencies. The depressed semicircle represents the charge-transfer resistance (R_{ct}) on electrolyte and the electrode interface, while the slope corresponds to the Li diffusion process inside the electrode material.[59,60] It is found that the diameter of the semicircle of Co_9S_8@NMCN nanocomposites is much smaller than that of Co_9S_8 nanoparticles, indicating that the R_{ct} value is smaller for Co_9S_8@NMCN nanocomposites, which is benefiting the diffusion kinetics upon cycling. Moreover, the phase angle of the slope for Co_9S_8 nanoparticles is ~40°, suggesting a diffusion-controlled feature of charging/discharging cycling. The phase angle of Co_9S_8@NMCN nanocomposites reaches 75°, indicating significant capacitive component upon cycling. The morphology change of the Co_9S_8@NMCN nanocomposites after cycling testing (80 cycles) is examined using SEM and

TEM (Fig. S9†). It is obvious that the morphology and size of Co_9S_8@NMCN nanocomposites are almost the same as in their initial state, demonstrating the good structural and morphological stabilities of the Co_9S_8@NMCN nanocomposites during charge/discharge cycling.

Based on the above results, the superior lithium storage properties of Co_9S_8@NMCN nanocomposites could be attributed to the synergistic effects of encapsulated Co_9S_8 nanoparticles, good electrical conductivity of NMCN, and micro/nanoarchitectures. First, the porous nature of the composites provides more free room to accommodate the local volume change upon charge/discharge cycling. NMCN can also give an elastic buffer space to accommodate the volume expansion/contraction of Co_9S_8 nanoparticles. Meanwhile, the micro/nanoarchitectures are beneficial for preventing the aggregation and keeping the integrity of the active materials. Second, the large specific surface area of the nanocomposites results from the porous space in NMCN and hierarchical structural nature can provide extra active sites for the storage of lithium ions, which is beneficial for increasing the specific capacity. Third, the nitrogen-doped carbon layers encapsulate each Co_9S_8 nanoparticle and form a continuous network. It can not only enhance the conductivity and efficient use of each Co_9S_8 nanoparticles in the composites, but also reduce the effective distance for lithium ions and electrons transport. The cooperation of these effects leads to the superior lithium storage of Co_9S_8@NMCN nanocomposites.

4. Conclusions

In summary, we have succeeded in constructing unique Co_9S_8@NMCN nanocomposites by a facile two-step strategy. The synthesis process involves the formation of ZIF-67 crystals and subsequent thermal annealing with sulfur powders in Ar atmosphere. Structural characterizations show that each Co_9S_8 nanoparticle is well encapsulated by nitrogen-doped carbon layers. When used as the anode materials for LIB, the Co_9S_8@NMCN nanocomposites delivered good lithium storage properties in terms of cycling stability, specific capacity, and rate capability. The composites exhibit a maximum specific capacity of 988 $mAhg^{-1}$ at a current density of 0.1 Ag^{-1} with outstanding charge/discharge rate capability and good cycling performance. Therefore, Co_9S_8@NMCN nanocomposites can be considered to be an attractive candidate as an anode material for LIBs. The present strategy can be extended to synthesize other metal sulfides/carbon nanocomposites that hold great promise in the field of energy storage and conversion.

Acknowledgements

This work was financially supported by National 973 Project of China (2015CB654902) and Chinese National Natural Science Foundation (1137417, 51390471, 51401114, 51527803). This work made use of the resources of the National Center for Electron Microscopy in Beijing and Tsinghua National Laboratory for Information Science and Technology.

Notes and references

[a] National Center for Electron Microscopy in Beijing, School of Materials Science and Engineering, The State Key Laboratory of New Ceramics and Fine Processing, Key Laboratory of Advanced Materials (MOE), Tsinghua University, Beijing 100084, People's Republic of China. E-mail: hsun@nanotech.dtu.dk; jzhu@mail.tsinghua.edu.cn

[b] Department of Micro- and Nanotechnology, Technical University of Denmark, 2800 Kongens Lyngby, Denmark

[c] Institute of Nuclear and New Energy Technology, Tsinghua University, Beijing 100084, China

[d] School of Metallurgy and Environment, Central South University, Changsha 410083, China

[e] Particles and Catalysis Research Group, School of Chemical Engineering, The University of New South Wales, Sydney, New South Wales 2052, Australia

[f] Department of Civil and Environmental Engineering, The Hong Kong University of Science and Technology, Hong Kong, China

† These authors contributed equally to this work.

Electronic Supplementary Information (ESI) available: [Additional SEM, TEM images, EDX pattern, XPS survey spectrum, XRD, TGA curves, and charge/discharge curves.]. See DOI: 10.1039/b000000x/

1 J. B. Goodenough and A. Manthiram, *MRS Commun*., 2014, **4**, 135.
2 C. Liu, F. Li, L. P. Ma and H. M. Cheng, *Adv. Mater*., 2010, **22**, 28.
3 V. L. Pushparaj, M. M. Shaijumon, A. Kumar, S. Murugesan, L. J. Ci, R. Vajtai, R. J. Linhardt, O. Nalamasu and P. M. Ajayan, *Proc. Natl. Acad. Sci. USA*, 2007, **104**, 13574.
4 S. Goriparti, E. Miele, F. De Angelis, E. Di Fabrizio, R. P. Zaccaria and C. Capiglia, *J. Power Sources.*, 2014, **257**, 421.
5 N. S. Choi, Z. H. Chen, S. A. Freunberger, X. L. Ji, Y. K. Sun, K. Amine, G. Yushin, L. F. Nazar, J. Cho and P. G. Bruce, *Angew. Chem. Int. Ed.*, 2012, **51**, 2.
6 M. Yoshio, H. Y. Wang, K. Fukuda, T. Umeno and T. Abeb, Z.Ogumi, *J. Mater. Chem*., 2004, **14**, 1754.
7 D. Yang, Z. Y. Lu, X. H. Rui, X. Huang, H. Li, J. X. Zhu, W. Y. Zhang, Y. M. Lam, H. H. Hng, H. Zhang, Q. Y. Yan. *Angew. Chem. Int. Ed.*, 2014, **53**, 9352.
8 G. W. Zhou, H. Li, H. P. Sun, D. P. Yu, Y. Q. Wang, X. J. Huang, L. Q. Chen, Z. Zhang, *Appl. Phys. Lett.*, 1999, **75**, 2447.
9 C. Eames and M. S. Islam, J. Am. Chem. Soc., 2014, **136**, 16270.
10 M. Naguib, J. Come, B. Dyatkin, V. Presser, P.-L. Taberna, P. Simon, M. W. Barsoum and Y. Gogotsi, *Electrochem. Commun*., 2012, **16**, 61.
11 Y. T. Gong, M. M. Li and Y. Wang, *ChemSusChem*, 2015, **8**, 931.
12 M. S. Balogun, W. T. Qiu, W. Wang, P. P. Fang, X. H. Lu and Y. X. Tong, *J. Mater. Chem. A*, 2015, **3**, 1364.
13 P. Poizot, S. Laruelle, S. Grugeon, L. Dupont and J. M. Tarascon, *Nature*, 2000, **407**, 496.
14 L. Zhang, L. Zhou, H. B. Wu, R. Xu and X. W. Lou, *Angew. Chem. Int. Ed*., 2012, **51**, 7267.
15 H. Hwang, H. Kim and J. Cho, *Nano Lett.*, 2011, **11**, 4826.
16 N. Mahmood, C. Zhang and Y. Hou, *Small*, 2013, **9**, 1321.
17 B. Luo, Y. Fang, B. Wang, J. Zhou, H. Song and L. Zhi, *Energy Environ. Sci.*, 2012, **5**, 5226.
18 D. Zhang, Y. J. Mai, J. Y. Xiang, X. H. Xia, Y. Q. Qiao and J. P. Tu, *J. Power Sources*, 2012, **217**, 229.
19 V. Etacheri, R. Marom, R. Elazari, G. Salitra and D. Aurbach, *Energy Environ. Sci*., 2011, **4**, 3243.
20 J. Wang, S. H. Ng, G. X. Wang, J. Chen, L. Zhao, Y. Chen and H. K. Liu, *J. Power Sources*, 2006, **159**, 287.
21 K. Brezesinski, J. Haetge, J. Wang, S. Mascotto, C. Reitz, A. Rein, S. H. Tolbert, J. Perlich, B. Dunn and T. Brezesinski, *Small*, 2011, **7**, 407.
22 J. Zhu, Z. Yin, D. Yang, T. Sun, H. Yu, H. E. Hoster, H. H. Hng, H. Zhang and Q. Yan, *Energy Environ. Sci*., 2013, **6**, 987.
23 M. V. Reddy, G. V. Subba Rao and B. V. R. Chowdari, *Chem. Rev*., 2013, **113**, 5364.

24 Q. F. Zhang, E. Uchaker, S. L. Candelaria and G. Z. Cao, *Chem. Soc. Rev.*, 2013, **42**, 3127.
25 P. G. Bruce, B. Scrosati and J. M. Tarascon, *Angew. Chem., Int. Ed.*, 2008, **47**, 2930.
26 Z. Wang, L. Pan, H. Hu and S. Zhao, *CrystEngComm*, 2010, **12**, 1899.
27 Y. Zhou, D. Yan, H. Xu, J. Feng, X. Jiang, J. Yue, J. Yang and Y. Qian, *Nano Energy*, 2015, **12**, 528.
28 S. Peng, X. Han, L. Li, Z. Zhu, F. Cheng, M. Srinivansan, S. Adams and S. Ramakrishna, *Small*, 2016, DOI: 10.1002/smll.201502788.
29 Y. N. Ko and Y. C. Kang, *Carbon*, 2015, **94**, 85.
30 H. Wang, S. Lu, Y. Chen, L. Han, J. Zhou, X. Wu and W. Qin, *J. Mater. Chem. A*, 2015, **3**, 23677.
31 R. Ramachandran, M. Saranya, C. Santhosh, V. Velmurugan, B. P. C. Raghupathy, S. K. Jeong and A. N. Grace, *RSC Adv.*, 2014, **4**, 21151.
32 G. Huang, T. Chen, Z. Wang, K. Chang and W. Chen, *J. Power Sources*, 2013, **235**, 122.
33 Y. G. Liu, Z. Y. Cheng, H. Y. Sun, J. P. Li, H. Arandiyan and M. Ahmad, *J. Power Sources*, 2015, **273**, 878.
34 Y. Y. Zhao, L. Kuai, Y. G. Liu, P. P. Wang, H. Arandiyan, S. F. Cao, J. Zhang, F. Y. Li, Q. Wang, B. Y. Geng and H. Y. Sun, *Sci. Rep*., 2015, **5**, 8722.
35 X. L. Wang, J. Mujtaba, F. Fang, M. Ahmad, H. Arandiyan, H. P. Yang, G. X. Sun and H. Y. Sun, *RSC Adv.*, 2015, **5**, 91574.
36 L. Bai, F. Fang, Y. Y. Zhao, Y. G. Liu, J. P. Li, G. Y. Huang and H. Y. Sun, *RSC Adv*., 2014, **4**, 43039.
37 H. Y. Sun, M. Ahmad, J. Luo, Y. Y. Shi, W. C. Shen and J. Zhu, *Mater. Res. Bull.*, 2014, **49**, 319.
38 K. S. Park, Z. Ni, A. P. Côté, J. Y. Choi, R. D. Huang, F. J. Uribe-Romo, H. K. Chae, M. O'Keeffe and O. M. Yaghi, *Proc Natl Acad Sci USA*. 2006, **103**, 10186.
39 A. Phan, C. J. Doonan, F. J. Uribe-Romo, C. B. Knobler, M. O'Keeffe and O. M. Yaghi, *Acc. Chem. Res.*, 2010, **43**, 58.
40 R. B. Wu, X. K. Qian, X. H. Rui, H. Liu, B. L. Yadian, K. Zhou, J. Wei, Q. Y. Yan, X.-Q. Feng, Y. Long, L. Y. Wang and Y. Z. Huang, *Small*, 2014, **10**, 1932.
41 P. Scherrer, *Ber. Verh. Saechs. Akad. Wiss. Leipzig*, *Math.-Phys. Kl.*, 1918, 26, 98.
42 Y. Waseda, E. Matsubara and K. Shinoda, *X-Ray Diffraction Crystallography: Introduction, Examples and Solved Problems*, Springer-Verlag Berlin Heidelberg, 2011, p. 125.
43 L. Shen, J. Wang, G. Xu, H. Li, H. Dou and X. Zhang, *Adv. Energy Mater*., 2015, **5**, 1400977.
44 B. X. Zhang, H. Gao and X. L. Li, *New J. Chem*. 2014, **38**, 4615.
45 L. L. Feng, G. D. Li, Y. Liu, Y. Wu, H. Chen, Y. Wang, Y. C. Zou, D. Wang and X. Zou, *ACS Appl. Mater. Interfaces*, 2015, **7**, 980.
46 W. Qin, L. Han, H. Bi, J. H. Jian, X. H. Wu and P. Gao, *Nanoscale*, 2015, **7,** 20180.
47 L. Lai, J. R. Potts, D. Zhan, L. Wang, C. K. Poh, C. Tang, H. Gong, Z. Shen, J. Lin and R. S. Ruoff, *Energy Environ. Sci.*, 2012, **5**, 7936.
48 D. H Guo, R. Shibuya, C. Akiba, S. Saji, T. Kondo and J. Nakamura, *Science*, 2016, **351**, 361.
49 Y. X. Zhou, H. B. Yao, Y. Wang, H. L. Liu, M. R. Gao, P. K. Shen and S. H. Yu, *Chem. Eur. J*., 2010, **16**, 12000.
50 R. C. Jin, J. H. Zhou, Y. S. Guan, H. Liu and G. Chen, *J. Mater. Chem. A*, 2014, **2**, 13241.
51 Y. Zhou, D. Yan, H. Xu, J. Feng, X. Jiang, J. Yue, J. Yang and Y. Qian, *Nano Energy*, 2015, **12**, 528.
52 Y. N. Ko, S. H. Choi, S. B. Park and Y. C. Kang, *Chem. Asian J*., 2014, **9**, 572.
53 Y. Zhou, D. Yan, H. Xu, S. Liu, J. Yang and Y. Qian, *Nanoscale*, 2015, **7**, 3520.
54 Y. Wang, J. Wu, Y. Tang, X. Lu, C. Yang, M. Qin, F. Huang, X. Li and X. Zhang, *ACS Appl. Mater. Interfaces*, 2012, **4**, 4246.
55 W. Shi, J. Zhu, X. Rui, X. Cao, C. Chen, H. Zhang, H. H. Hng and Q. Yan, *ACS Appl. Mater. Interfaces*, 2012, **4**, 2999.
56 G. Y. Huang, S. M. Xu, S. S. Lu, L. Y. Li and H. Y. Sun, *ACS Appl. Mater. Interfaces*, 2014, **6**, 7236.
57 Y. Mao, Q. Kong, B. Guo, X. Fang, X. Guo, L. Shen, M. Armand, Z. Wang and L. Chen, *Energy Environ. Sci*., 2011, **4**, 3442.
58 G. M. Zhou, D. W. Wang, F. Li, L. L. Zhang, N. Li, Z. S. Wu, L. Wen, G. Q. Lu and H. M. Cheng, *Chem. Mater*., 2010, **22**, 5306.
59 S. Zhang and P. Shi, *Electrochim. Acta*, 2004, **49**, 1475.
60 K. Fukuda, K. Kikuya, K. Isono and M. Yoshio, *J. Power Sources*, 1997, **69**, 165.

Graphic Abstract

Co_9S_8 nanoparticles encapsulated in nitrogen-doped mesoporous carbon networks have been successfully synthesized by annealing a cobalt containing metal organic framework with sulfur powders in Ar atmosphere. The resultant products exhibit excellent lithium storage properties.